PAPER

Check for updates

Comprehensive study of the structural, microstructural, and electrical properties of RbZnPO$_4$: insights into conduction mechanisms and the OLPT models

Imen Gharbi, [ID] [a] Arafet Ghoudi,[a] Najoua Weslati, [ID] [a] Mohamed Tliha[b] and Abderrazek Oueslati [ID] *[a]

The structural, microstructural, compositional, vibrational, and electrical properties of the rubidium zinc orthophosphate RbZnPO$_4$ compound have been comprehensively investigated. X-Ray powder diffraction (XRPD) confirmed the crystallization of RbZnPO$_4$ in a monoclinic system (space group $P2_1$), adopting a stuffed tridymite-type structure. Elemental analysis *via* energy-dispersive X-ray spectroscopy (EDS) confirmed the expected stoichiometry and homogeneous elemental distribution, while scanning electron microscopy (SEM) revealed a dense microstructure with submicron grain sizes ($\sim$0.4205 μm). Raman spectroscopy identified internal modes and external vibrational modes of the phosphate [PO$_4$]$^{3-}$ units, confirming the structural integrity of the phosphate framework. Impedance spectroscopy highlighted the semiconducting behavior of the RbZnPO$_4$ compound, with grain and grain boundary contributions effectively modeled using an equivalent circuit (R$_1$//CPE$_1$) + (R$_2$//CPE$_2$), where R and CPE represent the resistance and the Constant Phase Element, respectively. Temperature-dependent measurements revealed thermally activated conduction, characterized by negative temperature coefficient of resistance (NTCR) behavior. Activation energies for grains, grain boundaries, and total conduction were determined as 0.775, 1.173, and 0.581 eV, respectively. AC conductivity analyses further indicated frequency-dependent transport, consistent with the Overlapping Large Polaron Tunneling (OLPT) mechanism. The conduction mechanism has been thoroughly studied and well understood. These results demonstrate that RbZnPO$_4$ is a chemically stable, structurally well-defined, and electrically active phosphate, suitable for potential applications in thermally activated ionic or electronic conduction systems, such as sensors.

1. Introduction

The search for multifunctional materials with structural versatility and tunable transport properties has brought phosphate-based frameworks into focus. Among them, orthophosphates with the general formula A$^+$M^{2+}PO$_4$ (large A$^+$ = monovalent cation; small M^{2+} = Be, Mg, and Zn) adopting the stuffed tridymite structure have attracted increasing attention due to their open-framework architectures[1–6] and ferroic behavior.[7,8] These compounds combine corner-sharing MO$_4$ and PO$_4$ tetrahedra to form a three-dimensional network with tunnel-like voids that accommodate monovalent cations (*e.g.*, K$^+$, Tl$^+$, Rb$^+$,

and Cs$^+$),[8,9] facilitating ionic motion and creating promising candidates for electronic applications.

Despite their structural similarity, members of this family exhibit distinct ionic transport behaviors, governed by the size, mobility, and interactions of the tunnel-residing cations (A$^+$) as well as the rigidity of the host framework and the coordination of divalent cations.[2,3,10] For instance, RbMgPO$_4$ displays enhanced ionic conductivity, attributed to its flexible Mg-based lattice where a change in coordination is found and the formation of a super-lattice which encourages ion hopping.[10,11] However, the CsMgPO$_4$ incorporates a larger Cs$^+$ cation within a flexible Mg-based framework, showing moderate ionic conductivity. Although steric hindrance slightly restricts Cs$^+$ motion, the Mg framework retains some flexibility.[4,12] Conduction in CsMgPO$_4$ also fits the OLPT model, with hopping distances ranging from 1.54 Å to 2.78 Å.[12]

In comparison, KMgPO$_4$ and KZnPO$_4$ exhibit limited ionic conduction compared to RbMgPO$_4$ or CsMgPO$_4$, which can be attributed to K ions' relatively small size, low polarizability, and

[a] *Laboratory for Spectroscopic Characterization and Optics of Materials, Faculty of Sciences, University of Sfax, B. P. 1171, 3000 Sfax, Tunisia. E-mail: oueslatiabderrazek@yahoo.fr*

[b] *Department of Physics, Al-Qunfudah University College, Umm Al-Qura University, Saudi Arabia*

their higher activation energies and reduced carrier mobility.[13,14] These characteristics result in weaker dynamic disorder and narrower migration pathways within the tunnel structure. The latter hinders the mobility of the cations within the tunnel structure.[4] In the KMgPO$_4$, the conduction behavior follows the correlated barrier hopping (CBH) model before the phase transition and shifts to the non-overlapping small polaron tunneling (NSPT) model afterward.[13] In contrast, the conduction mechanism in α-KZnPO$_4$ is best described by the overlapping large polaron tunneling (OLPT) model, with an optimal polaron hopping distance ranging from 2.10 Å to 3.34 Å. This suggests a distinct charge transport regime that may allow for improved mobility.[14]

In contrast, CsZnPO$_4$ and TlZnPO$_4$ demonstrate more constrained ionic diffusion, likely influenced by steric hindrance and stronger electrostatic interactions, even though both undergo temperature-induced phase transitions accompanied by dielectric anomalies.[15,16]

The RbZnPO$_4$ compound has been previously studied, with initial studies focusing primarily on its crystal structure and the optical properties of rare-earth-doped variants incorporating Eu^{3+},[6] Dy^{3+},[17] and Sm^{3+} [18] ions. Building on prior studies of analogous orthophosphates such as (K, Rb, Cs)MgPO$_4$ and (K, Tl, Cs)ZnPO$_4$, the present work continues this line of research by focusing specifically on RbZnPO$_4$, aiming to further investigate its structural, microstructural, vibrational, and electrical properties, which remain insufficiently explored. Structural and microstructural analyses, combined with Raman spectroscopy and complex impedance spectroscopy, were employed to investigate the dominant ionic transport pathways in RbZnPO$_4$ and to extract key transport parameters governing its electrical behavior. These include the activation energy for ion migration, the optimum hopping distance (R_o), the density of states at the Fermi level ($N(E_F)$), and the spatial extent of the polaron. Together, these parameters provide critical insight into the charge transport regime and reveal how framework flexibility, cation size, and electronic structure jointly govern ionic conductivity in this class of open-framework phosphates.

In this context, the RbZnPO$_4$ compound emerges as an interesting candidate due to the intermediate size and moderate polarizability of the Rb$^+$ ion, which may offer a balance between mobility and structural stability. This balance is advantageous for applications such as thermally activated sensors, dielectric components, and low-temperature solid-state ionic conductors. Moreover, its structural analogy to previously studied high-conductivity phases (e.g., RbMgPO$_4$) suggests that RbZnPO$_4$ may harbor underexplored potential for optimized ionic transport. By elucidating the conduction mechanism and quantifying its transport parameters, this study aims to assess the viability of RbZnPO$_4$ in emerging electrochemical and sensing technologies.

2. Experimental details

2.1. Synthesis

The RbZnPO$_4$ compound was synthesized *via* a conventional solid-state reaction method, employing high-purity precursors,

namely Rb$_2$CO$_3$, ZnO, and (NH$_4$)$_2$HPO$_4$ ($\geq$99%, Sigma-Aldrich). The reagents were weighed according to stoichiometric ratios, thoroughly mixed, and ground in an agate mortar for 1 hour to ensure homogeneity. The resulting mixture was heated at 623 K for 8 hours, with the process being repeated multiple times and interspersed with intermediate grinding steps to enhance reaction completeness. The powder mass was monitored through repeated weighing until the target mass was achieved, indicating the complete release of volatile byproducts (NH$_3$, CO$_2$, and H$_2$O). The resulting powder was finely ground and then pressed into pellets 8 mm in diameter and 1.1 mm thick under a uniaxial pressure of 5 tons per cm^2. The pellets were subsequently calcined at 973 K for 10 hours and sintered at 1073 K for 2 hours to achieve phase formation and densification.

2.2. Device characterization

The XRPD was employed to identify the crystalline phases and refine the unit cell parameters of the RbZnPO$_4$ compound. The measurements were performed at room temperature using a Philips PW1710 diffractometer equipped with Cu Kα radiation (λ = 1.5406 Å), operating over a 2θ range of 10° to 85°. To ensure high-quality data, a total acquisition time of 12 hours was used, comprising 12 successive scans (1 hour per scan), and the resulting diffractogram corresponds to the cumulative sum of these scans. Rietveld profile refinement was carried out using the FullProf Suite,[19] enabling precise determination of lattice parameters and fitting quality without engaging in full structural refinement.

The morphology and elemental composition of the sample were analyzed using a Schottky field emission scanning electron microscope (SU5000 FE-SEM) equipped with an energy dispersive X-ray spectroscopy (EDS) system. High-resolution SEM imaging was employed to investigate the surface microstructure, while point EDS analysis and elemental mapping were conducted to determine the qualitative and spatial distribution of elements across the sample.

Raman spectroscopy was performed at room temperature using a T-64000 Horiba–Jobin–Yvon triple monochromator spectrometer. The measurements were carried out over a spectral range of 10–1200 cm^{-1} to investigate the vibrational modes of the studied compound.

Impedance spectroscopy measurements were conducted using a Solartron SI-1260 impedance/gain-phase analyzer in conjunction with a Solartron 1296 dielectric interface and a Linkam LTS420 temperature control system. Data was acquired using two distinct electrode configurations over a broad frequency range (1 to 10^5 Hz) across temperatures spanning from 513 K to 673 K.

3. Results and discussion

3.1. X-ray powder diffraction and polymorphism description

XRPD analysis confirmed that the RbZnPO$_4$ compound crystallizes in the monoclinic system, adopting the stuffed tridymite-type structure with the non-centrosymmetric space group $P2_1$. Fig. 1 displays the X-ray diffraction pattern, where all Bragg

peaks are correctly indexed and satisfactorily modeled, confirming the high quality of the structural refinement. The Rietveld refinement of the diffraction data at room temperature yielded the following lattice parameters: $a = 8.845$ Å, $b = 5.403$ Å, $c = 8.967$ Å, and a monoclinic angle $\beta = 89.749°$. A detailed analysis revealed that the unit cell parameters are consistent with previously reported values.[5,6] The quality of the refinement was assessed through the agreement factors, which were found to be $R_p = 4.66\%$, $R_{wp} = 6.01\%$, and $R_{exp} = 1.99\%$ (given in Table 1), indicating a satisfactory fit between the observed and calculated patterns. These structural results confirm the successful synthesis of phase-pure RbZnPO$_4$ and align with the framework topology typical of the tridymite-type phosphates.

The crystal structure of RbZnPO$_4$ adopts a regular stuffed tridymite-type framework, as clearly illustrated in the inset of Fig. 1, which was generated using Diamond software based on the crystallographic data reported by Shuangyu Xin *et al.*[6] In this structure, Zn^{2+} and P^{5+} atoms are tetrahedrally coordinated by oxygen atoms, forming a robust three-dimensional network of corner-sharing ZnO$_4$ and PO$_4$ tetrahedra. The arrangement of these tetrahedra forms distinct layers stacked along the *a*-axis. The superposition of these layers creates well-defined tunnels that run parallel to the *bc* plane. These tunnels are occupied by Rb$^+$ cations, which stabilize the anionic framework by compensating for the negative charge.

3.2. Elemental composition through energy dispersive X-ray spectroscopy (EDS)

The EDS spectrum at room temperature, shown in Fig. 2, exhibits distinct characteristic peaks corresponding to rubidium (Rb), zinc (Zn), phosphorus (P), and oxygen (O), which confirms the successful incorporation of all expected elements in the synthesized RbZnPO$_4$ compound. No impurity peaks are observed, indicating a high-purity phase without contamination,[20] making it suitable for further electrical and structural characterization.

Table 1 Crystallographic parameters of RbZnPO$_4$ refined from Rietveld analysis of XRPD data at room temperature

Formula	RbZnPO$_4$ at room temperature
Crystalline system	Monoclinic
Space group	$P2_1$
Lattice parameters	
a (Å)	8.845
b (Å)	5.403
c (Å)	8.967
β (°)	89.749
Refinement parameters	
R_p (%)/R_{wp} (%)/R_{exp} (%)	4.66/6.01/1.99

3.3. Microstructural analysis (SEM)

The SEM images at room temperature and different magnifications ($\times 2.00$k and $\times 5.00$k), shown in Fig. 3, reveal a dense polycrystalline microstructure composed of grains with irregular shapes and varying sizes. The presence of well-packed grains with limited visible porosity suggests efficient sintering during solid-state synthesis.[21] The grain size distribution, obtained through statistical analysis, exhibits a log-normal distribution with an average grain size of 0.4205 μm, indicating a predominantly submicron structure.[22,23] The distribution spans from 100 nm to 2.5 μm, revealing a mix of nano- and micro-scale grains. This variation in grain size can influence electrical transport by modifying grain boundary density and interfacial charge transport behavior.

The EDS elemental mapping for Rb (red), Zn (red), P (blue), and O (red) (bottom row of Fig. 3) provides valuable insights into the compositional uniformity of the synthesized RbZnPO$_4$ compound. The uniform intensity across the mapping area confirms that Rb is homogeneously distributed within the sample, while the presence of dispersed Zn points suggests a well-incorporated Zn phase without significant phase segregation. In addition, the P mapping also shows a uniform spread, which indicates a homogeneous phosphate network throughout the material. As for the O distribution, it is consistent with the expected stoichiometry of the phosphate phase, which further supports the integrity of the RbZnPO$_4$ compound.

The overall EDS results confirm that all elements are well-distributed without noticeable clustering or phase separation,[24]
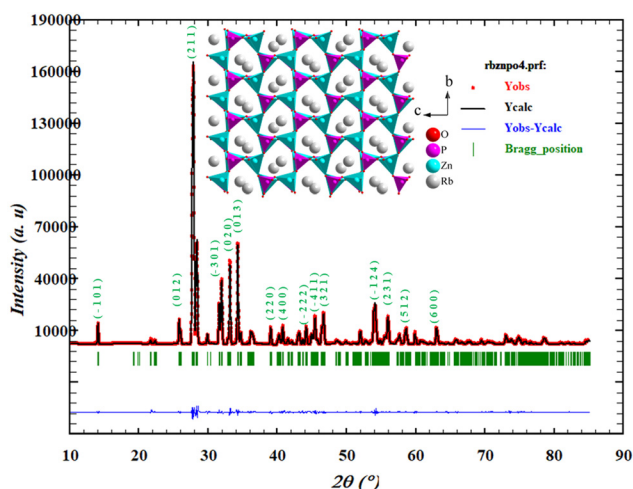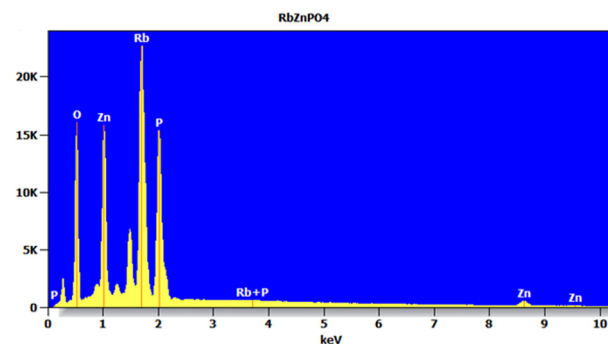

Fig. 1 Room-temperature Rietveld refinement of the X-ray powder diffraction pattern of RbZnPO$_4$ compound: experimental (red dotted), Calculated (black line), difference (blue), and Bragg Positions (green bars). Inset: Crystal structure projection along the *a*-axis showing the *bc*-plane.

Fig. 2 EDS spectrum and elemental composition of RbZnPO$_4$ recorded at room temperature, confirming the presence of Rb, Zn, P, and O.
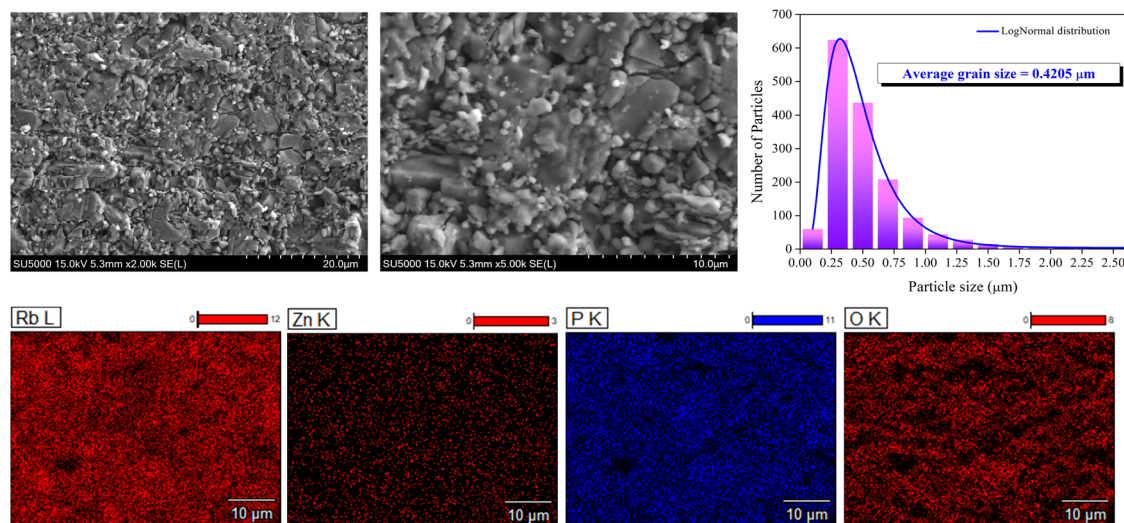
Fig. 3 Microstructural and compositional analysis of RbZnPO₄ synthesized by solid-state reaction and recorded at room temperature. (top left & middle) SEM images at different magnifications showing a polycrystalline microstructure. (top right) Grain size distribution fitted with a log-normal function, revealing an average grain size of 0.4205 μm. (bottom row) EDS elemental mapping of Rb, Zn, P, and O.

which is essential for maintaining consistent electrical properties throughout the sample.

3.4. Raman spectroscopy

The Raman spectra acquired at room temperature, covering the spectral range of 10–1200 cm^{-1}, are shown in Fig. 4. The observed vibrational bands identified in these spectra are compiled in Table 2, which provides a comprehensive list of their wavenumber values (in cm^{-1}), relative intensities, and mode assignments. The bands are categorized by intensity as very weak (vw), weak (w), medium (m), strong (s), very strong (vs), and shoulder (sh).

These bands are further classified into external and internal vibrations.[25] The low-wavenumber region (11.7–390.6 cm^{-1}) primarily corresponds to external modes which are mainly associated with the translational and rotational (librational) motions of the PO_4^{3-} tetrahedra, the Rb^+ and Zn^{2+} cations, and the interactions between these units.[15,16,25] The higher wavenumber region (415.4–1148.2 cm^{-1}) corresponds to internal modes and is associated with vibrations of the phosphate PO_4^{3-} group.[26] Notably, the bending (δ) and stretching (ν) vibrations of the PO_4^{3-} group are identified within the internal modes. The symmetric and asymmetric bending modes (δ_s and δ_{as}) appear between 415.4 and 499 cm^{-1} and between 552 and 725.4 cm^{-1}, respectively. The symmetric and asymmetric stretching modes (ν_s and ν_{as}) are observed in the range of 983.8–1008.4 cm^{-1} and 1023.5–1148.2 cm^{-1}, respectively.[27–31] These spectral features confirm the structural integrity of the phosphate units within the compound and provide valuable insight into the vibrational behavior of the RbZnPO₄ crystal lattice.
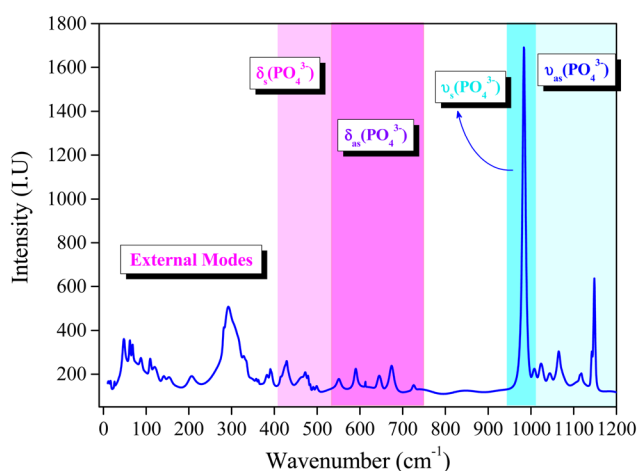
3.5. Electrical characterization (impedance spectroscopy)

Impedance spectroscopy was employed to investigate the electrical behavior of the RbZnPO₄ compound, and the complex electric modulus formalism was applied to gain deeper insight into its relaxation dynamics. Fig. 5 presents the complex modulus plots (M'' vs. M'), as well as the real (M') and imaginary (M'') parts of the modulus as a function of angular frequency, recorded over the temperature range 513–673 K.

The complex modulus plot shown in Fig. 5(a) reveals two overlapping arcs with depressed centers located below the real axis, characteristic of non-Debye relaxation behavior.[13,15] The shape of these arcs indicates the presence of two distinct dielectric relaxation processes, attributed to the contributions from grains and grain boundaries. The modulus formalism is particularly effective in highlighting such features due to its sensitivity to regions with lower capacitance, such as grains.[13,31]

As shown in Fig. 5(b), the real part of the modulus (M') exhibits typical dispersive behavior. Each curve features a low-

Fig. 4 Room-temperature Raman spectra of RbZnPO₄ recorded in the 10–1200 cm^{-1} Wavenumber range, showing vibrational modes of the $[PO_4]^{3-}$ tetrahedra.

Table 2 Assignment of Raman bands for the RbZnPO$_4$ compound

Band's wavenumber (cm^{-1})	Assignments
11.7 vw; 16.9 vw; 26.4 vw; 47.4 w; 62.2 w; 68.5 w; 87.7 w; 109.6 w; 120 sh; 141.3 w; 155 w; 208 w; 281.8 sh; 292.5 m; 329 sh; 334.6 sh; 357.8 vw; 363 vw; 382.5 sh; 390.6 w	External modes
415.4 vw; 428.4 w; 470.8 w; 499 vw	$\delta_s[PO_4]$ O–P–O
552 w; 590.6 w; 645.8 w; 673.8 w; 725.4 vw	$\delta_{as}[PO_4]$ O–P–O
983.8 vs; 1008.4 w	$\nu_s[PO_4]$ O–P
1023.5 w; 1044 w; 1065.3 w; 1117.5 w; 1142.5 sh; 1148.2 m	$\nu_{as}[PO_4]$ O–P

vw: very weak; sh: shoulder; m: medium; s: strong; vs: very strong; $\nu_{s,as}$: symmetric and asymmetric stretching modes; $\delta_{s,as}$: symmetric and asymmetric bending modes.

frequency plateau followed by a gradual increase and a high-frequency saturation region. With increasing temperature, the dispersion shifts toward higher frequencies, indicating a decrease in relaxation time and confirming the thermally activated nature of the relaxation processes.[14,33]

Fig. 5(c) presents the imaginary part of the modulus (M'') as a function of frequency. A broad asymmetric peak appears at each temperature and shifts to higher frequencies as the temperature increases, reflecting thermally activated charge carrier dynamics.[13,15] The broadness of the peak suggests the superposition of multiple relaxation processes. This feature

supports the presence of both grain and grain boundary contributions. To model this behavior, the M'' spectra were successfully fitted using a double Bergman function, which accurately captures the overlapping relaxation modes observed in the experimental data.[13,31,33]

Overall, the modulus analysis confirms the simultaneous contribution of grains and grain boundaries to the electrical response of RbZnPO$_4$. The observed non-Debye behavior, the temperature-dependent relaxation times, and the successful fitting using the double Bergman model provide strong evidence for multiple thermally activated relaxation mechanisms governed by localized charge carrier hopping.[13,14,31,32]

The Nyquist plot, shown in Fig. 6(a), exhibits two distinct semicircles, corresponding to the contributions from the grains (high-frequencies region) and grain boundaries (low-frequencies region).[32] Furthermore, the observed decrease in the diameters of the semicircles with increasing temperature indicates that the material's resistance decreases as the temperature rises, reflecting the NTCR behavior.[33,34] This trend is typical of thermally activated conduction mechanisms and confirms the semiconductor-like nature of the RbZnPO$_4$ compound.[11,35,36]

The experimental data were well-interpreted using an equivalent circuit model comprising two parallel branches, (R$_1$//CPE$_1$) + (R$_2$//CPE$_2$), where R$_1$//CPE$_1$ represents the grain resistance and constant phase element (fractal capacitance), and R$_2$//CPE$_2$ corresponds to the grain boundary resistance and constant phase element. To accurately reproduce the frequency-dependent impe-
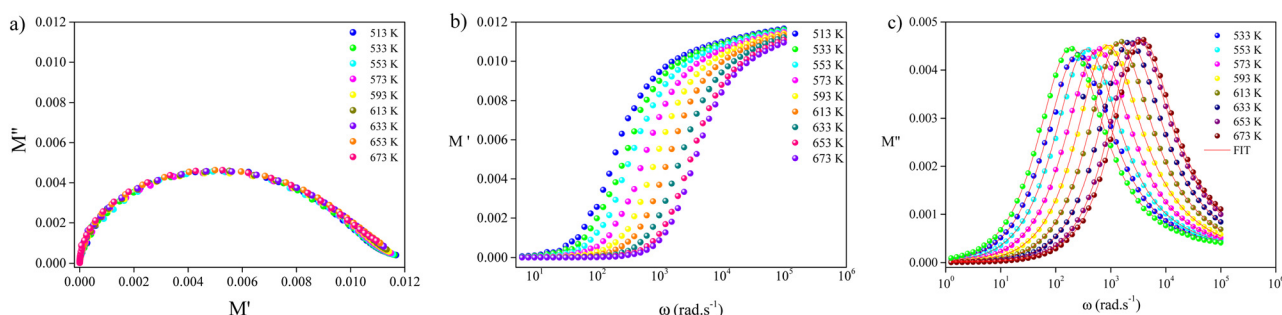
Fig. 5 Electrical modulus analysis of RbZnPO$_4$ in the 513–673 K temperature range. (a) Complex modulus plot (M'' vs. M'); (b) frequency dependence of modulus' (M') real part (c) Frequency dependence of modulus' (M'') imaginary part with fitted curves.
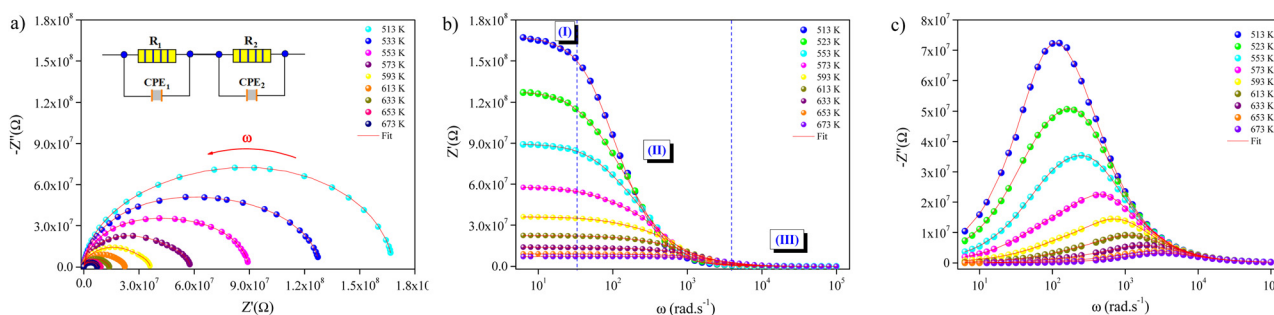
Fig. 6 (a) Nyquist plot of RbZnPO$_4$ in the 513–673 K temperature range (inset: equivalent circuit model used for data fitting (R$_1$//CPE$_1$ + R$_2$//CPE$_2$)), (b) Frequency dependence of real (Z') and (c) imaginary ($-Z''$) parts of complex impedance.

dance behavior, the real (Z') and imaginary $(-Z'')$ components were fitted using analytical expressions derived from this model. These expressions incorporate the frequency-dependent nature of the CPEs and are given by:

$$Z' = \frac{R_1\left(1 + R_1 Q_1 \omega^{\alpha_1} \cos\left(\alpha_1 \frac{\pi}{2}\right)\right)}{\left[1 + R_1 Q_1 \omega^{\alpha_1} \cos\left(\alpha_1 \frac{\pi}{2}\right)\right]^2 + \left[R_1 Q_1 \omega^{\alpha_1} \sin\left(\alpha_1 \frac{\pi}{2}\right)\right]^2}$$
$$+ \frac{R_2\left(1 + R_2 Q_2 \omega^{\alpha_2} \cos\left(\alpha_2 \frac{\pi}{2}\right)\right)}{\left[1 + R_2 Q_2 \omega^{\alpha_2} \cos\left(\alpha_2 \frac{\pi}{2}\right)\right]^2 + \left[R_2 Q_2 \omega^{\alpha_2} \sin\left(\alpha_2 \frac{\pi}{2}\right)\right]^2} \quad (1)$$

$$-Z'' = \frac{R_1^2 Q_1 \omega^{\alpha_1} \sin\left(\alpha_1 \frac{\pi}{2}\right)}{\left[1 + R_1 Q_1 \omega^{\alpha_1} \cos\left(\alpha_1 \frac{\pi}{2}\right)\right]^2 + \left[R_1 Q_1 \omega^{\alpha_1} \sin\left(\alpha_1 \frac{\pi}{2}\right)\right]^2}$$
$$+ \frac{R_2^2 Q_2 \omega^{\alpha_2} \sin\left(\alpha_2 \frac{\pi}{2}\right)}{\left[1 + R_2 Q_2 \omega^{\alpha_2} \cos\left(\alpha_2 \frac{\pi}{2}\right)\right]^2 + \left[R_2 Q_2 \omega^{\alpha_2} \sin\left(\alpha_2 \frac{\pi}{2}\right)\right]^2} \quad (2)$$

These formulations allow for precise modeling of the impedance spectra, accounting for the non-ideal capacitive behavior observed in both the grain and grain boundaries. They reinforce the interpretation derived from the Nyquist plots and support the reliability of the equivalent circuit approach used.

The frequency dependence of the real (Z') and imaginary $(-Z'')$ parts of the complex impedance, respectively shown in Fig. 6(b) and (c), provides valuable insights into the charge transport and relaxation mechanisms within the material. As shown in Fig. 6(b), (Z') exhibits a high value in the low-frequency region, particularly at lower temperatures, reflecting the dominant contribution of grain boundary resistance and possible space charge accumulation.[37] With increasing frequency, (Z') gradually decreases due to the reduced contribution of interfacial polarization and the dominant role of grain conduction at higher frequencies, where charge carriers can no longer follow the rapidly oscillating electric field.[38] At high frequencies, (Z') reaches a nearly constant minimum value that systematically decreases with temperature, suggesting enhanced electrical conductivity due to thermally activated charge carriers.[35]

Meanwhile, the imaginary part $(-Z'')$, shown in Fig. 6(c), displays a well-defined relaxation peak at each temperature. The peak shifts toward higher frequencies and decreases in magnitude with increasing temperature, indicating a thermally activated relaxation process with shorter relaxation times at elevated temperatures. The absence of multiple peaks suggests the dominance of a single relaxation mechanism, likely associated with the grain boundary effect, which generally occurs in the low-frequency region. The asymmetric and broadened nature of the peak points to a non-Debye relaxation behavior,[15,39,40] which is consistent with the use of constant phase elements in the equivalent circuit model. Overall, these findings corroborate the semiconducting behavior of the material and the efficient conduction across grains and grain boundaries at higher temperatures.

To quantitatively support these interpretations, a detailed analysis of the extracted resistance and capacitance values *versus* temperature was performed. Bar plots of these parameters are presented in Fig. 7. As illustrated, both the grain resistance (R_1) and grain boundary resistance (R_2), shown in Fig. 7(a) and (b), respectively, decrease significantly with increasing temperature. This behavior is characteristic of semiconducting materials, where thermal activation enhances charge carrier mobility.[41] In contrast, the capacitance values of the constant phase element CPE $(Q_1$ and $Q_2)$, depicted in Fig. 7(c) and (d), exhibit a notable increase with temperature. This increase can be attributed to enhanced dielectric polarization and thermally activated dipolar or space charge contributions. These observations indicate improved charge storage capability and increased interfacial polarization at elevated temperatures. Overall, the results highlight the effective thermal activation of conduction and polarization mechanisms and suggest the presence of relatively low interfacial barriers, as inferred from the Nyquist analysis.[42]

To gain deeper insight into the relaxation mechanisms underlying the observed impedance behavior, the imaginary part of the impedance $(-Z'')$ was further analyzed using the distribution of relaxation times (DRT) method at the studied temperature range, as presented in Fig. 8. The DRT $(-Z''_{\max}$ *versus* $\log_{10}(\tau))$ spectrum reveals a broad and asymmetric distribution of relaxation processes. The increase of $(-Z''_{\max})$ with the increase of $\log_{10}(\tau)$ suggests that slower, more resistive relaxation mechanisms are likely governed by grain boundaries. This relationship underscores the non-ideal, thermally activated, and heterogeneous nature of electrical relaxation in the material[43] and can be effectively described using the DRT formalism.[44,45]

The temperature dependence of the DC conductivity for grains (σ_G), grain boundaries (σ_{GB}), and total conductivity (σ_{TOT}) was evaluated using the extracted parameters from the equivalent circuit model, and the results are depicted in Fig. 9. These conductivities were calculated, at the studied temperature range, using the following relations:[46]

$$\sigma_G = \frac{e}{S \cdot R_1} \quad (3)$$

$$\sigma_{GB} = \frac{e}{S \cdot R_2} \times \frac{C_1}{C_2} \quad (4)$$

$$\sigma_{tot} = \frac{e}{S \cdot (R_1 + R_2)} \quad (5)$$

where is the sample's thickness, R is the resistance (R_1 for grains, R_2 for grain boundaries), S is the surface area of the measured pellet, and C is the capacitance (C_1 for grains, C_2 for grain boundaries).
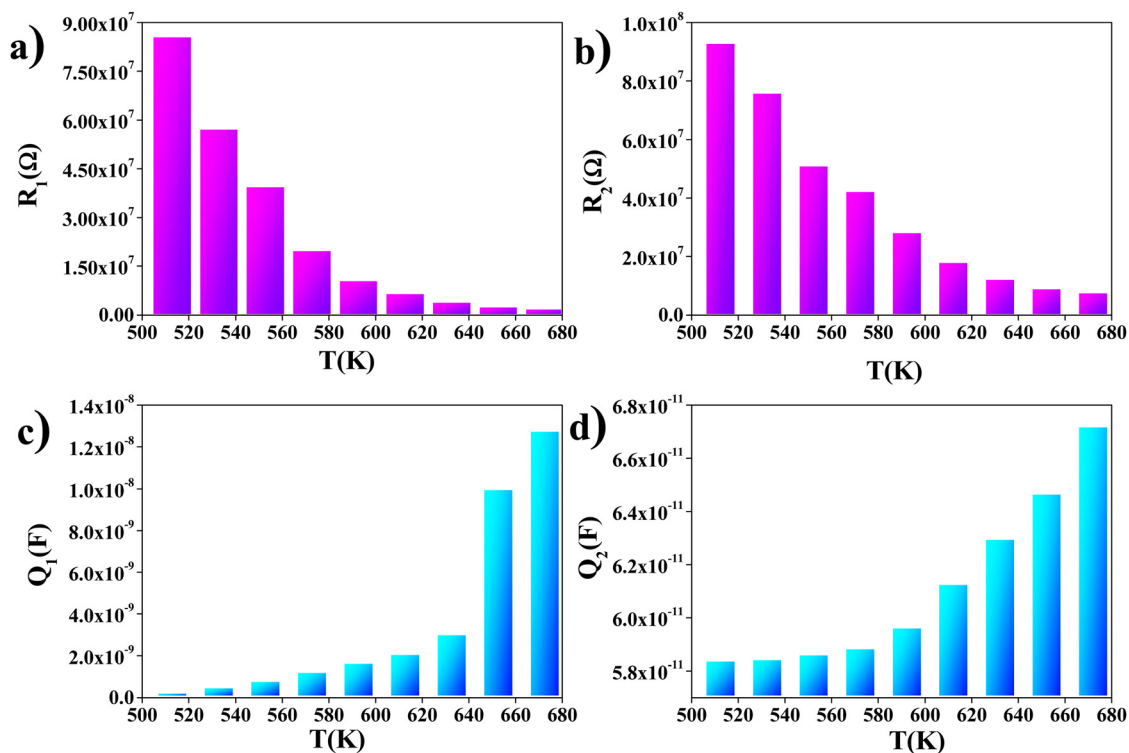
Fig. 7 Temperature dependence of the resistance and constant phase element (CPE) parameters extracted from Nyquist plot fittings: (a) grain resistance R_1, (b) grain boundary resistance R_2, (c) grain CPE capacitance Q_1, and (d) grain boundary CPE capacitance Q_2.
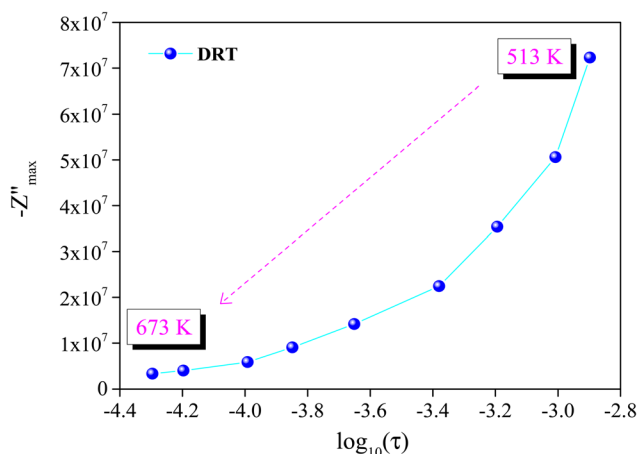

Fig. 8 Variation of peak imaginary impedance ($-Z''_{max}$) vs. log(τ) at different temperatures, showing relaxation distribution from DRT analysis for RbZnPO$_4$.

The grains and grain boundaries' pure capacitance are determined using the following equation:[15]

$$C_{1,2} = R_{1,2}^{\frac{1-\alpha_{1,2}}{\alpha_{1,2}}} \times Q_{1,2}^{\frac{1}{\alpha_{1,2}}} \quad (6)$$

where Q is the capacitance of the constant phase element CPE and α is the fractal exponent.

The Arrhenius plots of ln(σ) *versus* 1000/T exhibit linear behavior for all components, confirming the thermally activated nature of the conduction processes. Grains, grain boundaries, and total activation energies (E_G, E_{GB}, and E_{TOT}) were estimated from the slopes of the linear fits according to the Arrhenius equation:[47]

$$\sigma_{G, GB, tot} = \sigma_0 \exp\left(-\frac{E_{G, GB, TOT}}{k_B T}\right) \quad (7)$$

where σ_0 is the pre-exponential factor and k_B is the Boltzmann constant.
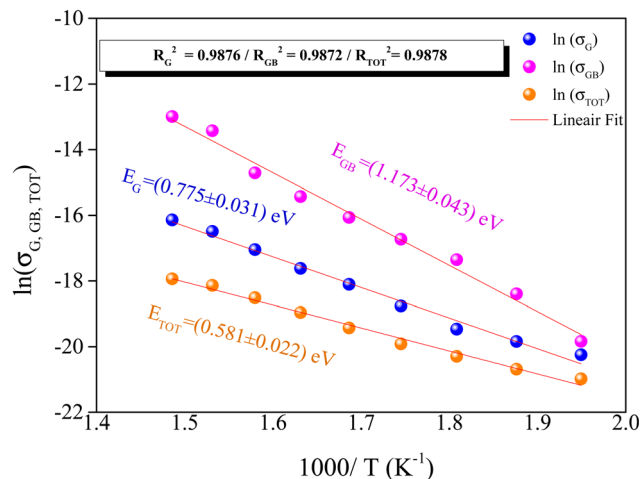
Fig. 9 Arrhenius plots of grain, grain boundary, and total conductivity (ln($\sigma_{G,GB,TOT}$)) *versus* (1000/T), confirming NTCR behavior and determining the activation energies.

The activation energies were found to be (0.775 ± 0.031) eV for grains, (1.173 ± 0.043) eV for grain boundaries, and (0.581 ± 0.022) eV for the total conductivity. These results indicate that grain boundaries exhibit a higher energy barrier for charge transport from grains, reflecting their more resistive nature. The lower activation energy of the total conductivity suggests that the overall conduction is dominated by the grains' contribution, especially at higher temperatures.

This analysis reinforces the conclusions drawn from the impedance spectra, showing that grain boundaries strongly block charge movement at low temperatures. In contrast, grain conductivity becomes dominant as thermal activation increases. The good linearity of the Arrhenius plots further validates the reliability of the equivalent circuit model used to extract the resistance values.

To gain deeper insights into the conduction mechanisms of the RbZnPO$_4$ compound, the variation of AC conductivity (σ_{AC}) *versus* angular frequency (ω) was investigated and presented in Fig. 10. In the measured frequency and temperature range, it is observed that AC conductivity increases with both temperature and frequency. This behavior further supports the NTCR characteristics and the semiconducting properties of the RbZnPO$_4$ compound.[48] In addition, two distinct regimes are evident. At low frequencies, the AC conductivity exhibits a frequency-independent plateau, commonly known as DC conductivity. In this regime, the applied electric field is unable to disrupt the hopping process, and the long-range mobilizations of charge carriers are responsible for such a plateau region. At higher frequencies, the AC conductivity values converge and become nearly temperature-independent, indicating that charge transport is less influenced by thermal activation. This high-frequency dispersion region reflects the localized nature of AC conductivity, primarily associated with short-range hopping of charge carriers.[48] The fit curves, shown in red, align well with the experimental data, confirming the validity of Jonscher's power-law expression, which is the following:[15,46]

$$\sigma_{AC} = \frac{\sigma_s}{1+\tau^2\omega^2} + \frac{\sigma_\infty\tau^2\omega^2}{1+\tau^2\omega^2} + A\omega^s \quad (8)$$

where σ_s denotes the low-frequency conductivity, σ_∞ represents the estimated high-frequency conductivity, ω is the angular frequency, τ is the relaxation time, A is a temperature-dependent pre-factor, and s is the power-law exponent ($0 < s < 2$) that reflects the degree of interaction between mobile ions and their surrounding environment.[11,49]

To better understand the conduction process at the microscopic level and to accurately interpret the AC conductivity behavior of the studied material, several theoretical models have been considered to describe how charge carriers move through disordered or flexible frameworks under an alternating electric field. In the quantum mechanical tunneling (QMT) model, charge carriers tunnel through potential barriers without requiring thermal activation, resulting in a temperature-independent frequency exponent $s(T)$. In contrast, the correlated barrier hopping (CBH) model assumes that carriers hop between localized states over energy barriers, with the exponent $s(T)$ decreasing as temperature increases due to enhanced thermal activation. The non-overlapping small polaron
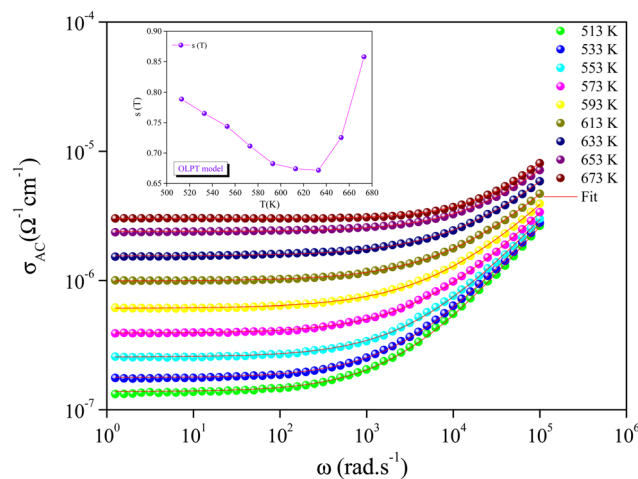

Fig. 10 Frequency dependence of AC conductivity (σ_{AC}) *versus* angular frequency (ω). Inset: Temperature dependence of the frequency exponent $s(T)$, showing non-monotonic behavior consistent with OLPT model.

tunneling (NSPT) model involves localized charge carriers (small polarons) tunneling between isolated sites without wavefunction overlap, leading to a frequency exponent $s(T)$ that increases with rising temperature. Finally, the overlapping large polaron tunneling (OLPT) model describes charge transport *via* large, spatially extended polarons whose wavefunctions overlap between sites; in this case, $s(T)$ exhibits a non-monotonic behavior, first decreasing with temperature to reach a minimum, and then increasing again. This distinct temperature dependence of $s(T)$ serves as a key diagnostic for identifying the dominant conduction mechanism in a given material.[50]

The temperature dependence of the frequency exponent $s(T)$, derived from the Jonscher power law, is presented in the inset of Fig. 10. The behavior of the frequency exponent $s(T)$ exhibits a decrease as the temperature increases, reaching a minimum around 633 K, then increases with the increase of temperature. This non-monotonic trend suggests that the conduction mechanism is consistent with the OLPT model.

According to the derived model, the exponent $s(T)$ is given by the following expression:[15,31]

$$s(T) = 1 - \frac{8\alpha R_\omega + \frac{6W_{H0}r_p}{R_\omega k_B T}}{\left(2\alpha R_\omega + \frac{W_{H0}r_p}{R_\omega k_B T}\right)^2} \quad (9)$$

where α denotes the polaron spatial extension, W_{H0} is the polaron hopping energy, r_p represents the polaron radius, k_B is the Boltzmann constant, and R_ω corresponds to the optimum hopping distance.

The AC conductivity $\sigma_{AC}(\omega)$ was determined using the theoretical expression:[31]

$$\sigma_{AC}(\omega) = \frac{\pi^4 e^2 (k_B T)^2 N(E_F)^2}{12} \times \frac{\omega(R_\omega)^4}{\left(2\alpha k_B T + \frac{W_{H0}r_p}{(R_\omega)^2}\right)} \quad (10)$$

where $N(E_F)$ represents the density of states at the Fermi level.

The optimal hopping distance R_ω (or hopping length) is calculated at a fixed frequency ω by solving the following equation:[15,31]

$$R_\omega = \frac{1}{4\alpha} \left\{ \left[\left(\frac{W_{H0}}{k_B T} + \ln(\omega\tau_0) \right)^2 + \frac{8\alpha W_{H0} r_p}{k_B T} \right]^{1/2} - \left(\ln(\omega\tau_0) + \frac{W_{H0}}{k_B T} \right) \right\} \quad (11)$$

where τ_0 refers to the relaxation time.

This calculation is closely related to the logarithmic variation of the AC conductivity ($\ln \sigma_{AC}$) as a function of the inverse temperature ($1000/T$) at various frequencies. As shown in Fig. 11, this variation exhibits a thermally activated behavior characterized by a series of nearly linear curves. This behavior indicates that the conduction mechanism is governed by temperature-dependent activation processes.[51] The AC conductivity increases with increasing frequency, which consists of a hopping-type mechanism involving localized charge carriers.[52] The successful fitting of this behavior using the OLPT model further supports the interpretation that the charge transport in the studied material occurs via tunneling of large polarons between overlapping potential wells.[53] The parameters extracted from the fitting procedure are summarized in Table 3.

According to the OLPT model, the frequency dependence of both conductivity and activation energy arises from the enhanced tunneling probability at higher frequencies, which facilitates polaron movement and leads to a reduction in activation energy.[53,54] The good agreement between experimental data and the fitting confirms the relevance of this model in describing the conduction process in this system, likely linked to the disordered nature or structural flexibility of the material.[55] In the present case, the studied compound adopts a stuffed tridymite-type structure with monoclinic symmetry ($P2_1$ space group), a framework known for its inherent structural flexibility and dynamic disorder, especially due to the rotation and distortion of PO_4 and ZnO_4 tetrahedral units. Such features promote local potential fluctuations and enhance the

Table 3 Fitting parameters of the experimental AC conductivity data using the OLPT model

Frequency (Hz)	$N(E_F)$ ($\times 10^{16}$)	α (Å^{-1}) ($\times 10^{-3}$)	W_{H0} (eV)	r_p (Å)
100	1.331	5.69	1.542	3.455
500	1.537	4.66	1.570	3.513
1000	1.500	4.06	1.582	3.554
5000	1.579	3.73	1.653	3.636
10 000	1.745	2.85	1.751	3.802
15 000	1.821	0.255	1.780	3.867

overlap of polaron wavefunctions, thereby facilitating the tunneling process described by the OLPT mechanism.

Fig. 12(a) displays the variation of the density of states at the Fermi level, $N(E_F)$, and the tunneling parameter α versus frequency, within the framework of the OLPT model. It is observed that $N(E_F)$ increases with frequency, indicating enhanced availability of localized states contributing to the conduction process. However, α decreases as the frequency increases, indicating that the effective tunneling distance of polarons shortens due to enhanced wavefunction overlap. This trend supports the notion that the conduction mechanism is driven by polaron hopping, with tunneling enhanced at higher frequencies.

Fig. 12(b) shows the variation of the optimum hopping distance R_ω versus temperature for selected frequencies. The
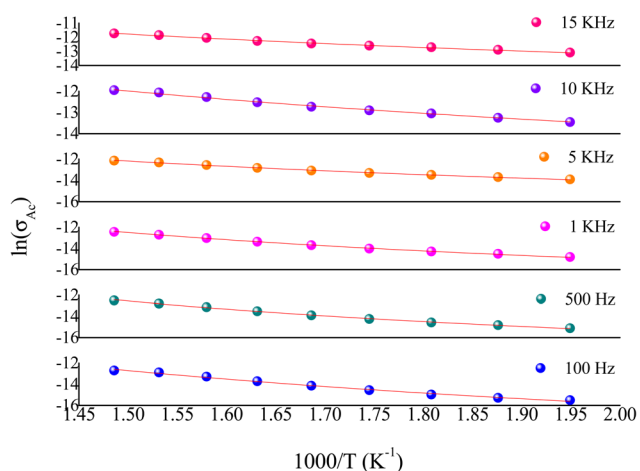
Fig. 11 Fitting of AC conductivity data at different frequencies using the OLPT model, demonstrating the frequency and temperature-dependent polaron hopping behavior.
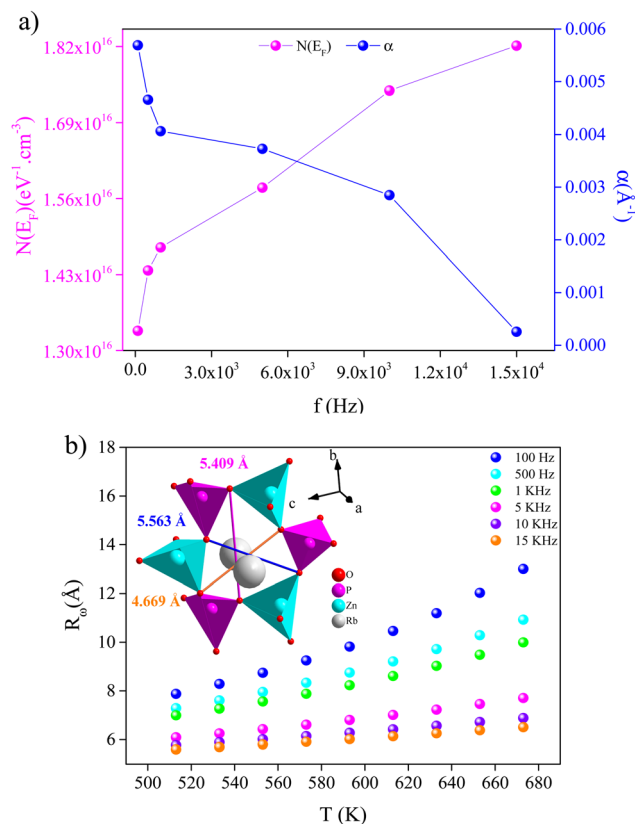
Fig. 12 Variation of (a) α (Å^{-1}) and $N(E_F)$ (eV^{-1} cm^{-3}) according to the frequency (OLPT model) and (b) temperature-dependence of the tunneling distance R_ω (Å) at different frequencies, supporting the large polaron conduction mechanism.

inset depicts the dimensions of the structural tunnels within the stuffed tridymite-type framework, which range from 4.669 Å to 5.563 Å. The calculated R_ω values, lying between 5.5 Å and 13 Å, are comparable to or larger than the tunnel dimensions, particularly at lower frequencies and higher temperatures. This indicates that the charge transport mechanism involves polaron hopping over spatial distances that are relevant to the structural features of the material. The fact that R_ω exceeds the tunnel size, at lower frequencies and higher temperatures, supports the notion that large polarons tunnel between spatially proximate localized states either within or across adjacent tunnels. Furthermore, the observed decrease in tunneling distance with increasing frequency implies a shift in the transport mechanism, suggesting that charge carriers progressively transition from long-range to short-range tunneling mechanisms.[56]

4. Conclusions

In this study, the $RbZnPO_4$ compound was successfully synthesized via solid-state reaction and characterized using a suite of complementary techniques. X-ray powder diffraction confirmed the formation of a phase-pure monoclinic structure of the stuffed tridymite type, with well-refined lattice parameters and a satisfactory Rietveld fit. Elemental analysis through EDS validated the expected stoichiometry and purity of the synthesized compound, while SEM micrographs revealed a dense microstructure composed of submicron grains with homogeneous elemental distribution. Raman spectroscopy provided further confirmation of the structural integrity, showcasing characteristic external and internal vibrational modes of the phosphate network.

Impedance spectroscopy results highlighted the semiconducting nature of $RbZnPO_4$, exhibiting typical NTCR behavior and non-Debye relaxation. The electrical response was dominated by grain boundary effects at low temperatures and transitioned toward grain-dominated conduction at higher temperatures. The thermally activated charge transport was determined through Arrhenius analysis, which revealed higher activation energy for grain boundaries compared to grains. AC conductivity analysis, supported by Jonscher's power law and the OLPT model, confirmed that conduction occurs via thermally activated hopping mechanisms involving localized carriers.

Overall, the structural and electrical investigations presented in this work establish $RbZnPO_4$ as a stable and promising candidate for potential applications in thermally activated ionic or electronic conduction systems, such as sensors or energy storage devices.

Conflicts of interest

The authors declare that they have no known competing financial interests or personal relationships that could have appeared to influence the work reported in this paper.

Data availability

The authors confirm that the data used to support the findings of this study are included within the article and are available from the corresponding author upon reasonable request.

The complete output of the Rietveld refinement performed using the FullProf Suite on the XRPD data of the $RbZnPO_4$ compound. It includes refinement parameters, background and peak shape coefficients, unit cell parameters, and statistical indicators such as R_p, R_{wp}, R_{exp}, and χ^2 values. This file provides transparency regarding the profile fitting procedure and supports the structural analysis presented in the manuscript. See DOI: https://doi.org/10.1039/d5ma00506j

Acknowledgements

References

1 R. Masse and A. Durif, Contribution to the crystal chemistry of $M^I M^{II} PO_4$ monophosphates (M^I = K, Rb, Cs; M^{II} = Be), J. Solid State Chem., 1988, **73**(2), 468–472, DOI: 10.1016/0022-4596(88)90132-6.

2 G. Wallez, S. Jaulmes, A. Elfakir and M. Quarton, Stereochemical Activity of Thallium(I) Lone Pair in the Tridymite-Related Compounds $TlBePO_4$ and $TlBeAsO_4$, J. Solid State Chem., 1995, **114**(1), 123–128, DOI: 10.1006/jssc.1995.1018.

3 R. Ait Benhamou, G. Wallez, P. Loiseau, B. Viana, M. Elaatmani, M. Daoud and A. Zegzouti, Polymorphism of new rubidium magnesium monophosphate, J. Solid State Chem., 2010, **183**(9), 2082–2086, DOI: 10.1016/j.jssc.2010.07.016.

4 R. Yu, H. Li, H. Ma, C. Wang and H. Wang, Structure-dependent luminescence properties of Eu^{3+}-doped $CsBPO_4$ (B = Mg, Zn), Solid State Sci., 2014, **29**, 34–40, DOI: 10.1016/j.solidstatesciences.2013.12.017.

5 L. Elammari and B. Elouadi, Structure cristalline de $RbZnPO_4$, J. Chim. Phys., 1991, **88**, 1969–1974, DOI: 10.1051/jcp/1991881969.

6 S. Xin, Y. Wang, G. Zhu, X. Ding, W. Geng and Q. Wang, Structure- and temperature-sensitive photoluminescence in a novel phosphate red phosphor $RbZnPO_4$:Eu^{3+}, Dalton Trans., 2015, **44**(36), 16099–16106, DOI: 10.1039/c5dt02099a.

7 B. Elouadi and L. Elammari, Crystal structures and ferroelectric properties of $A^I B^{II} PO_4$(A^I = monovalent cation and B^{II} = divalent cation), Ferroelectrics, 1990, **107**(1), 253–258, DOI: 10.1080/00150199008221547.

8 D. Blum, J. C. Peuzin and J. Y. Henry, $MM'PO_4$, a new family of ferroic compounds, Ferroelectrics, 1984, **61**(1), 265–279, DOI: 10.1080/00150198408018940.

9 D. Blum, A. Durif and M. T. Averbuch-pouchot, Crystal structures of the three forms of $CsZnPO_4$, Ferroelectrics, 1986, **69**(1), 283–292, DOI: 10.1080/00150198608008201.

10 I. Gharbi, A. Oueslati, A. Bulou and M. Gargouri, Using Raman spectroscopy and structural properties in understanding the ferroelectric nature of the $RbMgPO_4$ phase transitions, *Mater. Res. Bull.*, 2021, **139**, 111250, DOI: **10.1016/j.materresbull.2021.111250**.

11 I. Gharbi, A. Oueslati and K. Guidara, Alternating current conduction mechanisms of $RbMgPO_4$ compound, *Mater. Res. Bull.*, 2018, **100**, 1–6, DOI: **10.1016/j.materresbull.2017.11.058**.

12 I. Gharbi, M. H. Dhaou, A. Oueslati and M. Gargouri, Synthesis and investigation on the morphological, structural, and electrical proprieties of a cesium magnesium phosphate prepared using solid-state reaction, *J. Mater. Sci.: Mater. Electron.*, 2023, **34**(10), 1–13, DOI: **10.1007/s10854-023-10288-y**.

13 L. Miladi, A. Oueslati and K. Guidara, Phase transition, conduction mechanism and modulus study of $KMgPO_4$ compound, *RSC Adv.*, 2016, **6**(86), 83280–83287, DOI: **10.1039/c6ra18560f**.

14 N. Chakchouk, Kh. B. Brahim, M. B. Gzaiel and A. Oueslati, Investigation of optical and electrical properties of the semiconducting α-$KZnPO_4$ compound, *RSC Adv.*, 2022, **12**(11), 6831–6840, DOI: **10.1039/d2ra00426g**.

15 I. Gharbi, A. Oueslati, K. Guidara and B. Louati, Ionic conductivity and conduction mechanism of $CsZnPO_4$ compound, *Ionics*, 2019, **25**(8), 3991–4001, DOI: **10.1007/s11581-019-02954-1**.

16 I. Gharbi, A. Oueslati, M. H. Dhaou and M. Gargouri, Investigation of ferroelectric phase transitions in $TlZnPO_4$ stuffed tridymite compound, *J. Solid State Chem.*, 2022, **308**, 122886, DOI: **10.1016/j.jssc.2022.122886**.

17 G. Zhu and S. Xin, A novel blue light pumped yellow-emitting phosphor RbZnPO4:Dy^{3+}with satisfactory color tuning and thermal properties for high-power warm white light emitting diodes, *RSC Adv.*, 2015, **5**(129), 106795, DOI: **10.1039/c5ra24286**.

18 G. Zhu, C. Wang, S. Xin and S. Yuan, The synthesis, electronic structure and photoluminescence property investigation of temperature sensitive red phosphors $RbZnPO_4$:Sm^{3+}, *Mater. Res. Bull.*, 2017, **92**, 99–103, DOI: **10.1016/j.materresbull.2017.04.006**.

19 R. A. Young, P. E. Mackie and R. B. von Dreele, Application of the pattern-fitting structure-refinement method of X-ray powder diffractometer patterns, *J. Appl. Crystallogr.*, 1977, **10**(4), 262–269, DOI: **10.1107/s0021889877013466**.

20 A. Kumar, S. Dutta, S. Kim, T. Kwon, S. S. Patil, N. Kumari, S. Jeevanandham and I. S. Lee, Solid-State Reaction Synthesis of Nanoscale Materials: Strategies and Applications, *Chem. Rev.*, 2022, **122**(15), 12748–12863, DOI: **10.1021/acs.chemrev.1c00637**.

21 J. Zheng and J. S. Reed, Effects of Particle Packing Characteristics on Solid-State Sintering, *J. Am. Ceram. Soc.*, 1989, **72**(5), 810–817, DOI: **10.1111/j.1151-2916.1989.tb06222.x**. Portico. .

22 C.-Y. Chang, C.-Y. Huang, Y.-C. Wu, C.-Y. Su and C.-L. Huang, Synthesis of submicron $BaTiO_3$ particles by modified solid-state reaction method, *J. Alloys Compd.*, 2010, **495**(1), 108–112, DOI: **10.1016/j.jallcom.2010.01.096**.

23 L. N. Lau, K. P. Lim, A. N. Ishak, M. M. Awang Kechik, S. K. Chen, N. B. Ibrahim, M. Miryala, M. Murakami and A. H. Shaari, The Physical Properties of Submicron and Nano-Grained $La_{0.7}Sr_{0.3}MnO_3$ and $Nd_{0.7}Sr_{0.3}MnO_3$ Synthesised by Sol–Gel and Solid-State Reaction Methods, *Coatings*, 2021, **11**(3), 361, DOI: **10.3390/coatings11030361**.

24 D. E. Newbury and N. W. M. Ritchie, Elemental mapping of microstructures by scanning electron microscopy-energy dispersive X-ray spectrometry (SEM-EDS): extraordinary advances with the silicon drift detector (SDD, *J. Anal. At. Spectrom.*, 2013, **28**(7), 973, DOI: **10.1039/c3ja50026h**.

25 A. V. Peschanskii and A. Yu Glamazda, Computational and spectroscopic comparative analysis of Raman phonon spectra of $LiNiPO_4$, *Low Temp. Phys.*, 2024, **50**(7), 589–595, DOI: **10.1063/10.0026325**.

26 N. Membreño, P. Xiao, K.-S. Park, J. B. Goodenough, G. Henkelman and K. J. Stevenson, *In Situ* Raman Study of Phase Stability of α-$Li_3V_2(PO_4)_3$ upon Thermal and Laser Heating, *J. Phys. Chem. C*, 2013, **117**(23), 11994–12002, DOI: **10.1021/jp403282a**.

27 I. L. Botto and M. Vassallo, The vibrational spectrum of the $NaZnPO_4$ ferroelectric phase, *J. Mater. Sci. Lett.*, 1989, **8**(11), 1336–1337, DOI: **10.1007/bf00721513**.

28 E. Y. Borovikova, V. Kurazhkovskaya, D. Ksenofontov, Y. Kabalov, V. Pet'kov and E. Asabina, Relationship between IR spectra and crystal structures of β-tridymite-like CsM_2 + PO_4 compounds, *Eur. J. Mineral.*, 2012, **24**(5), 777–782, DOI: **10.1127/0935-1221/2012/0024-2209**.

29 O. García-Moreno, M. Alvarez-Vega, F. García-Alvarado, J. García-Jaca, J. M. Gallardo-Amores, M. L. Sanjuán and U. Amador, Influence of the Structure on the Electrochemical Performance of Lithium Transition Metal Phosphates as Cathodic Materials in Rechargeable Lithium Batteries: A New High-Pressure Form of $LiMPO_4$ (M = Fe and Ni), *Chem. Mater.*, 2001, **13**(5), 1570–1576, DOI: **10.1021/cm000596p**.

30 F. Shi and E.-C. Xiao, Sintering behavior, crystal structures, phonon characteristics and dielectric properties of $LiZnPO_4$ microwave dielectric ceramics, *Mater. Chem. Phys.*, 2021, **259**, 124139, DOI: **10.1016/j.matchemphys.2020.124139**.

31 N. Chakchouk, B. Louati and K. Guidara, Electrical properties and conduction mechanism study by OLPT model of $NaZnPO_4$ compound, *Mater. Res. Bull.*, 2018, **99**, 52–60, DOI: **10.1016/j.materresbull.2017.10.046**.

32 J. R. Macdonald and W. B. Johnson, Fundamentals of Impedance Spectroscopy, *Impedance Spectroscopy*, 2005, pp. 1–26, Portico , DOI: **10.1002/0471716243.ch1**.

33 Y. Pu, Z. Dong, P. Zhang, Y. Wu, J. Zhao and Y. Luo, Dielectric, complex impedance and electrical conductivity studies of the multiferroic $Sr_2FeSi_2O_7$-crystallized glass-ceramics, *J. Alloys Compd.*, 2016, **672**, 64–71, DOI: **10.1016/j.jallcom.2016.02.137**.

34 M. Abbassi, R. Ternane, I. Sobrados, A. Madani, M. Trabelsi-Ayadi and J. Sanz, Ionic conductivity of apatite-type solid electrolyte ceramics $Ca_{2-x}Ba_xLa_4Bi_4(SiO_4)_6O_2$ ($0 \leq x \leq 2$), *Ceram. Int.*, 2013, **39**(8), 9215–9221, DOI: **10.1016/j.ceramint.2013.05.026**.

35 F. Tayari, S. S. Teixeira, M. P. F. Graça, M. Essid and K. I. Nassar, Investigating structural, dielectric, and electrical characteristics of sol–gel synthesized perovskite ceramic $Bi_{0.7}Ba_{0.3}(FeTi)_{0.5}O_3$, *J. Sol-Gel Sci. Technol.*, 2024, **112**(2), 601–613, DOI: **10.1007/s10971-024-06549-9**.

36 C. Xu, J. Chen, G. Feng, Z. Chen, W. Yang, C. Yang, O. Shmatova, Y.-S. Hu and J. Zhao, A novel KTP-type $NaTiPO_4F$ electrode material for high-performance Na-ion batteries, *Energy Storage Mater.*, 2025, **76**, 104156, DOI: **10.1016/j.ensm.2025.104156**.

37 M. Ben Gzaiel, I. Garoui, F. N. Almutairi, I. Mbarek and A. Oueslati, Lead-Free halide perovskites for optoelectronic application: Investigation of structural, optical, electric and dielectric behaviors, *Opt. Mater.*, 2024, **154**, 115664, DOI: **10.1016/j.optmat.2024.115664**.

38 *Impedance Spectroscopy*, ed. E. Barsoukov and J. R. Macdonald, 2005, DOI: **10.1002/0471716243**.

39 Y. Ben Taher, A. Oueslati, N. K. Maaloul, K. Khirouni and M. Gargouri, Conductivity study and correlated barrier hopping (CBH) conduction mechanism in diphosphate compound, *Appl. Phys. A: Mater. Sci. Process.*, 2015, **120**(4), 1537–1543, DOI: **10.1007/s00339-015-9353-3**.

40 M. Shah, M. Nadeem, M. Idrees, M. Atif and M. J. Akhtar, Change of conduction mechanism in the impedance of grain boundaries in $Pr_{0.4}Ca_{0.6}MnO_3$, *J. Magn. Magn. Mater.*, 2013, **332**, 61–66, DOI: **10.1016/j.jmmm.2012.12.015**.

41 A. Ghoudi, I. Chaabane, R. Naouari, A. Aydi, A. Oueslati, E. Dhahri, B. F. O. Costa, T. Nikitin, J. A. Paixão and R. Fausto, Optical and electric properties of the organic–inorganic hybrid bis(2-amino-5-picolinium) Tetrachlorocobaltate(II) $[(C_6H_9N_2)_2\text{-}CoCl_4]$, *Inorg. Chem. Commun.*, 2024, **168**, 112925, DOI: **10.1016/j.inoche.2024.112925**.

42 H. Rahmouni, M. Smari, B. Cherif, E. Dhahri and K. Khirouni, Conduction mechanism, impedance spectroscopic investigation and dielectric behavior of $La_{0.5}Ca_{0.5-x}Ag_xMnO_3$ manganites with compositions below the concentration limit of silver solubility in perovskites ($0 \leq x \leq 0.2$), *Dalton Trans.*, 2015, **44**(22), 10457–10466, DOI: **10.1039/c5dt00444f**.

43 A. K. Jonscher (n.d.), The universal dielectric response. Annual Conference on Electrical Insulation and Dielectric Phenomena, pp. 23–40, DOI: **10.1109/ceidp.1990.201316**.

44 E. IVERS-TIFFÉE and A. WEBER, Evaluation of electrochemical impedance spectra by the distribution of relaxation times, *J. Ceram. Soc. Jpn.*, 2017, **125**(4), 193–201, DOI: **10.2109/jcersj2.16267**.

45 M. A. Danzer, Generalized Distribution of Relaxation Times Analysis for the Characterization of Impedance Spectra, *Batteries*, 2019, **5**(3), 53, DOI: **10.3390/batteries5030053**.

46 M. Megdiche, C. Perrin-pellegrino and M. Gargouri, Conduction mechanism study by overlapping large-polaron tunnelling model in $SrNiP_2O_7$ ceramic compound, *J. Alloys Compd.*, 2014, **584**, 209–215, DOI: **10.1016/j.jallcom.2013.09.021**.

47 M. Ajili, I. Gharbi and A. Oueslati, Synthesis, morphological, and ionic conduction studies of a copper potassium phosphate compound, *Ionics*, 2022, **29**(1), 353–361, DOI: **10.1007/s11581-022-04791-1**.

48 S. Sahoo, L. Sahoo, N. C. Nayak, B. N. Parida and R. K. Parida, Investigation of the structural, dielectric, magnetic properties and NTC-thermistor response of $CaBiFeMnO_6$ double perovskites, *Mater. Adv.*, 2024, **5**(13), 5442–5457, DOI: **10.1039/d4ma00175c**.

49 S. Ben Yahya, I. Garoui, M. Zaghrioui, A. Oueslati and B. Louati, Solid-state synthesized Li_4GeO_4 germanate: an exploration of its structure, vibrational characteristics, electrical conductivity, and dielectric properties, *RSC Adv.*, 2025, **15**(12), 9295–9304, DOI: **10.1039/d5ra01165e**.

50 S. Nasri, A. Jraba, I. Garoui, A. Oueslati and E. Elaloui, Potassium tin chloride (K_2SnCl_6) as a lead-free perovskite: anti-solvent synthesis, structural characterization, and charge transport properties, *RSC Adv.*, 2025, **15**(7), 5369–5380, DOI: **10.1039/d5ra00090d**.

51 S. R. Elliott, A.c. conduction in amorphous chalcogenide and pnictide semiconductors, *Adv. Phys.*, 1987, **36**(2), 135–217, DOI: **10.1080/00018738700101971**.

52 A. K. Jonscher, The 'universal' dielectric response, *Nature*, 1977, **267**(5613), 673–679, DOI: **10.1038/267673a0**.

53 A. R. Long, Frequency-dependent loss in amorphous semiconductors, *Adv. Phys.*, 1982, **31**(5), 553–637, DOI: **10.1080/00018738200101418**.

54 K. Funke, Jump relaxation in solid electrolytes, *Prog. Solid State Chem.*, 1993, **22**(2), 111–195, DOI: **10.1016/0079-6786(93)90002-9**.

55 D. L. Sidebottom, Universal Approach for Scaling the ac Conductivity in Ionic Glasses, *Phys. Rev. Lett.*, 1999, **82**(18), 3653–3656, DOI: **10.1103/physrevlett.82.3653**.

56 M. Ben Bechir and M. H. Dhaou, Study of charge transfer mechanism and dielectric relaxation of all-inorganic perovskite $CsSnCl_3$, *RSC Adv.*, 2021, **11**(35), 21767–21780, DOI: **10.1039/d1ra02457d**.